

DOI: 10.1002/sml.200500436

Room-Temperature Ferromagnetism in Doped Face-Centered Cubic Fe Nanoparticles

Bingqing Wei,* Mutsuhiro Shima,* Ranjit Pati, Saroj K. Nayak,* David J. Singh, Renzhi Ma, Yubao Li, Yoshio Bando, Saburo Nasu, and Pulickel M. Ajayan*

The magnetism of Fe and its alloys has been at the center of scientific and technological interest for decades. Along with the ferromagnetic nature of body-centered cubic Fe, the magnetic properties of face-centered cubic (fcc) Fe have attracted much attention. It is well known that fcc Fe is thermodynamically unstable at ambient conditions and not ferromagnetic. Contrary to what is known, we report that elongated nanoparticles of fcc Fe, grown within graphitic nanotubes, remain structurally stable and appear ferromagnetic at room temperature. The magnetic moment ($2 \pm 0.5 \mu_B$) in these nanoparticles and the hyperfine fields for two different components of ^{57}Fe (33 and 21 T), measured by Mössbauer spectroscopy, are explained by carbon interstitials in the expanded fcc Fe lattice, that is, FeC_x where $x \approx 0.10$, which result in the formation of a dominant Fe_4C stoichiometry. First-principles calculations suggest that the ferromagnetism observed in the fcc Fe is related to both lattice expansion and charge transfer between iron and carbon. The understanding of strain- and dopant-induced ferromagnetism in the fcc Fe could lead to the development of new fcc Fe-based alloys for magnetic applications.

Keywords:

- carbon nanotubes
- doping
- ferromagnetism
- iron
- nanoparticles

1. Introduction

It is well known that both pure face-centered cubic (fcc) γ -phase Fe and the fcc Fe-C phase, austenite, are thermody-

namically metastable at ambient conditions and not ferromagnetic.^[1–11] However, theoretical studies have predicted the existence of two different magnetic states in γ -Fe: a ferromagnetic (or high-spin) state and an antiferromagnetic (or low-spin) state,^[7] which depend on the lattice parameter.^[3–6] Attempts have been made in the past to stabilize γ -

[*] Prof. B. Wei

Department of Electrical and Computer Engineering
and Center for Computation and Technology
Louisiana State University, Baton Rouge, LA 70803 (USA)
Fax: (+1) 225-578-5538
E-mail: weib@ece.lsu.edu

Prof. B. Wei, Prof. M. Shima, Prof. P. M. Ajayan
Department of Materials Science and Engineering
Rensselaer Polytechnic Institute, Troy, NY 12180 (USA)
E-mail: shima@rpi.edu
ajayan@rpi.edu

Prof. R. Pati, Prof. S. K. Nayak
Department of Physics, Applied Physics, and Astronomy
Rensselaer Polytechnic Institute, Troy, NY 12180 (USA)
E-mail: nayak@rpi.edu

Dr. D. J. Singh
Materials Science and Technology Division
Oak Ridge National Laboratory, Oak Ridge TN 37831-6032 (USA)
Dr. R. Ma, Dr. Y. Li, Prof. Y. Bando
National Institute for Materials Science
Advanced Materials Laboratory
Tsukuba, Ibaraki 305-004 (Japan)
Prof. S. Nasu
Division of Materials Physics, Department of Physical Science
Osaka University, Toyonaka, Osaka 560-8531 (Japan)

Fe at room temperature by either reducing the dimensions of specimens or by incorporating carbon atoms into the lattice. These have resulted in ferromagnetic fcc Fe confined to a thickness of only a few monolayers.^[9,10] The theoretically predicted magnetic transition from low-spin to high-spin states in fcc Fe provides insight into complex magnetic phenomena observed in fcc Fe-based alloys, such as the invar effect.^[12,13]

Herein, we report that elongated nanoparticles of fcc Fe can be grown within graphitic nanotubes by vapor-phase interaction of ferrocene and hydrocarbons, and that they remain structurally stable and appear ferromagnetic at room temperature. The elongated Fe nanoparticles so produced are encapsulated within graphitic layers and, thus, are both protected from easy oxidization and effectively shielded from magnetostatic interactions that may otherwise arise between particles.^[14] Previously, it has been suggested that ferromagnetism in the samples arises from body-centered cubic (bcc) Fe.^[14–16] Our careful study, reported here, indicates that the Fe nanoparticles exist primarily in the fcc phase and are ferromagnetic at room temperature. First-principles calculations suggest that the ferromagnetism observed in these fcc Fe nanoparticles is related to lattice expansion and charge transfer between Fe and C.

2. Results and Discussion

Aligned arrays of multiwalled carbon nanotubes (CNTs) trap large numbers of Fe nanoparticles in their hollow cores during synthesis.^[17] The encapsulated Fe nanoparticles are anisotropic in morphology, as shown by the TEM image in Figure 1a, and are 5–10 nm in diameter and 10–150 nm in length (along the tube axis). HRTEM observations (300-kV field-emission microscope with a wavelength of 0.01966 Å), together with selected-area diffraction and nanodiffraction patterns taken from tens of individual nanoparticles, identified all the nanoparticles as fcc Fe. A typical lattice image of the fcc Fe is shown in Figure 1b, with intersected atomic planes (lattice fringes) marked (111) and $(\bar{1}\bar{1}1)$. The corresponding electron diffraction pattern is shown as the inset of Figure 1b, which is a typical $[1\bar{1}0]$ zone axis diffraction of an fcc iron crystal. In addition, the clearly resolved lattice images and electron diffraction patterns taken from the γ -Fe particles show that the (111) plane of γ -Fe is always parallel to the (002) plane of the nanotubes, which indicates the existence of an orientational relationship between the γ -Fe nanoparticles and the CNT walls. The structure of the iron nanoparticles in the bulk sample was also confirmed to be fcc Fe by X-ray diffraction analysis (Figure 1c; CuK α radiation with a wavelength of 1.5405 Å, 40 kV and 40 mA). A lattice parameter of 0.362–0.364 nm is obtained from the X-ray measurements as well as from electron diffraction. This value is larger than the lattice parameter of fcc Fe stabilized in Cu,^[18] which has a helical spin-spiral ground state. In fact, TEM measurements were carried out throughout the sample area. All particles checked showed fcc diffraction patterns. We did not find any bcc Fe, nor did we find any cementite (DO₁₁) or hP8 Fe₃C. This finding is consistent

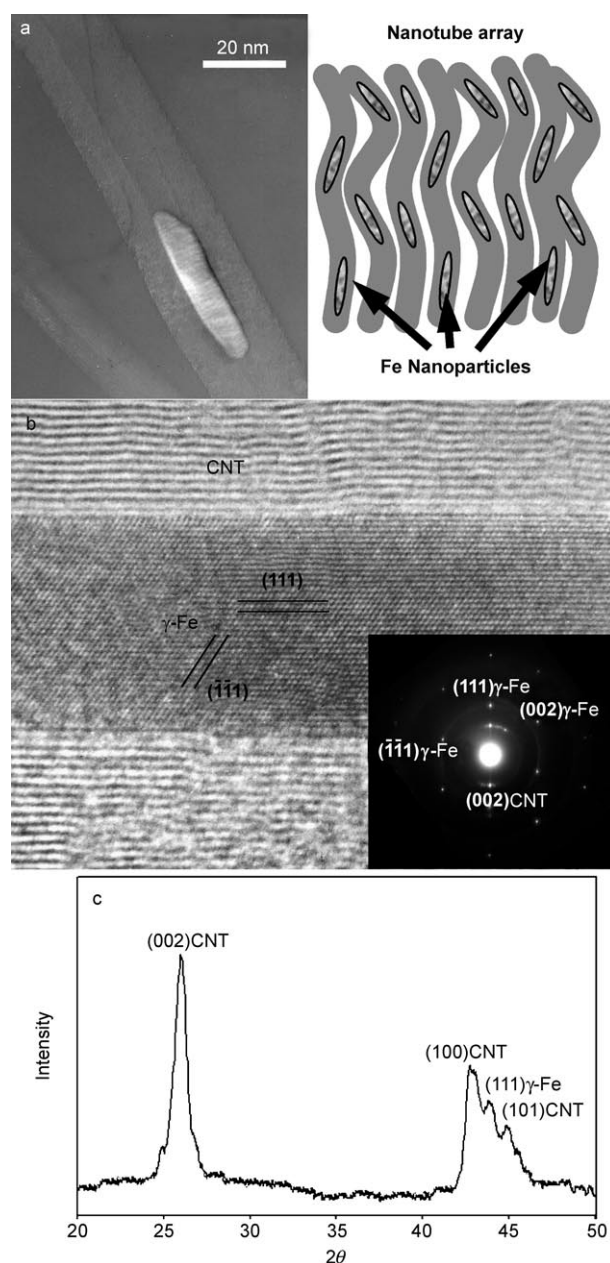


Figure 1. Structural characterization of nanoparticles trapped inside vertically aligned carbon nanotube films. a) Typical TEM image of elongated nanosized catalyst (Fe here) trapped inside the central cavity of a nanotube which was grown on a SiO₂ substrate by chemical vapor deposition. The trapped anisotropic nanoparticles of Fe form a metal array embedded in the whole nanotube forest, as shown by the schematic. b) HRTEM image of the two-dimensional lattice of Fe nanoparticles trapped inside the nanotube cavity. The Fe particle is identified as fcc Fe from the selected-area diffraction pattern (see inset), which is a typical $[1\bar{1}0]$ zone axis diffraction of an fcc Fe crystal. The (111) is the most packed plane in fcc Fe and is parallel to the (002) plane of the nanotubes. The parallel between fcc Fe(111) and CNT(002) agrees perfectly with epitaxial growth. The contrast in the Fe lattice is attributed to strains induced by either the interstitial carbon atoms or the coherence between the nanoparticle and the graphite wall. c) X-ray spectrum taken from the nanotube forests, which shows the existence of fcc γ -Fe with a lattice parameter of 3.62–3.64 Å.

with other recent observations of trapped fcc Fe nanoparticles synthesized using similar methods, but no magnetic studies have been reported on these structures to date.^[19,20]

The phase diagram of Fe–C^[21] shows that γ -Fe is thermodynamically stable at 800 °C and normally might experience phase transitions during a cooling process to room temperature, to give α -Fe, Fe₃C, or a mixture of them depending on its composition. With a saturated C atom and a constrained force from the CNTs which trap the γ -Fe nanoparticles, the phase transitions might be retarded or inhibited owing to a rapid cooling rate for the nanosized γ -Fe particles, that is, quenching of the γ -Fe nanoparticles by the flowing Ar gas in our chemical vapor deposition (CVD) process. As a result of different cooling rates, the phase transitions to α -Fe, Fe₃C, or a mixture thereof could also occur, as reported by other researchers.^[14–16]

The magnetic properties of the Fe nanoparticle arrays were measured at room temperature in an applied field (H) of up to 0.5 T by using an alternating-gradient magnetometer (AGM). The experimental results shown in Figure 2a demonstrate the ferromagnetic behavior of the materials. Both sets of results (magnetic fields in parallel and perpendicular to the tube axis) exhibit a sheared hysteresis loop around zero field, where the magnetization is saturated for the field above 0.4 T. Their squareness M_r/M_s and coercivity H_c are 0.59 and 85 mT in the parallel direction and 0.48 and 67 mT in the perpendicular direction, respectively, which suggests the existence of slightly unidirectional magnetic anisotropy, presumably due to the “imperfect” alignment of the elongated shape of iron nanoparticles embedded in the wiggly nanotubes and perhaps lattice strain in the fcc Fe nanoparticles. The non-observation of bcc Fe and analysis of the Mössbauer data (below) show that the measured magnetization comes from the trapped fcc iron nanoparticles.

To gain atomistic-level insights into the origin of the magnetic moment observed, ⁵⁷Fe Mössbauer-effect measurements were carried out at various temperatures between 300 and 5 K. Figure 2b shows the Mössbauer spectrum observed at 300 K. According to our analysis, the spectrum contains four sets of patterns: Fe-(1) and Fe-(2) correspond to hyperfine-field splittings with $H_{in}=33$ T (2.2 μ B per Fe) and 21 T (1.4 μ B per Fe), respectively, which originate from ferromagnetic iron atoms; Fe-(3) represents a broad singlet originating from antiferromagnetic (low-spin state) γ -Fe; and FeO_x corresponds to a wide hyperfine-field splitting with $H_{in}=49$ T from residual iron oxides, presumably formed during sample preparation. On the basis of the Mössbauer intensity ratio, we began with a model of a supercell with a plane of fcc Fe₄C separated by two planes of pure fcc Fe, and assumed that Fe-(1) and Fe-(2) are associated with Fe atoms in the Fe₄C lattice at the corners and face-centered positions of the fcc unit cell, as schematically illustrated in Figure 2b. Based on the relative percentage of spectrum area for $H_{in}=33$ T (41%) and 21 T (26%), we suggest that high-spin-state Fe-(1) atoms located at the corner positions of both the pure fcc (no carbon) and Fe₄C unit cells are the major contribution (41%) to the observed ferromagnetism, along with intermediate-spin-state Fe-(2)

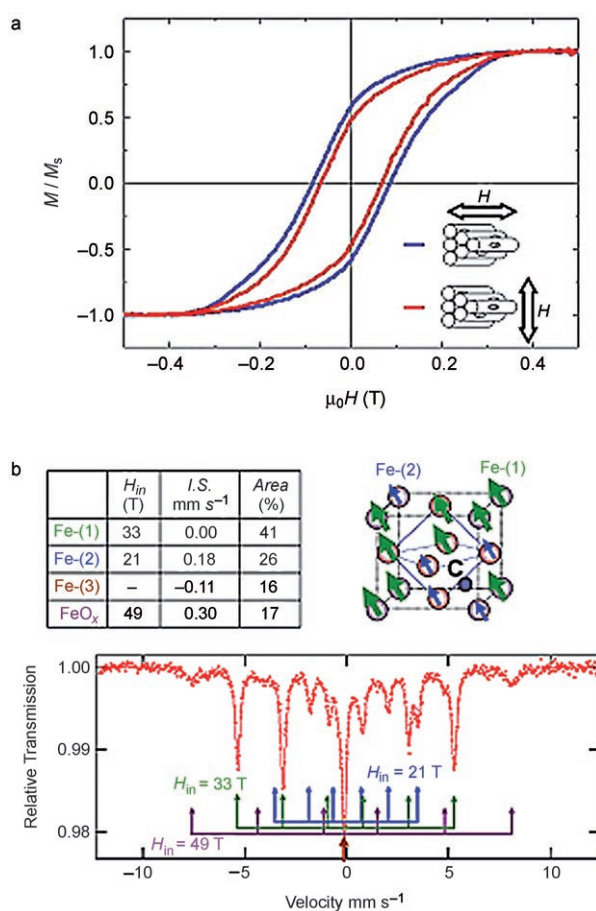


Figure 2. Magnetic properties of Fe nanoparticles trapped inside carbon nanotube films. a) Magnetic hysteresis curves for a CNT sample containing iron nanoparticles; the blue and the red loops represent the data obtained when a magnetic field was applied along and normal to the axis of the CNTs, respectively. b) ⁵⁷Fe Mössbauer spectrum of the iron nanoparticles measured at room temperature. Four different states were obtained: Fe-(1) for Fe at the corners of the fcc Fe₄C lattice, Fe-(2) for the face-centered positions of fcc Fe₄C, Fe-(3) for pure fcc Fe, and FeO_x for iron oxides. The corresponding hyperfine field (H_{in}), isomer shift (I.S.), and relative percentage of the spectrum area estimated from the measured data are shown in the inset table.

atoms (26%) at the face-centered positions only within the Fe₄C unit cell (see Figure 2b). Indeed, a very similar magnetic structure has been found in fcc Fe₄N, where a nitrogen atom is incorporated at the octahedral interstitial site in the fcc unit cell and the hyperfine fields for Fe atoms at the corner and face-centered positions are 34 and 22 T, respectively.^[22]

Mössbauer and field-cooling (FC)/zero-field-cooling (ZFC) magnetization measurements at low temperatures have been reported on CNT samples containing bcc Fe, fcc Fe, and Fe₃C, and it was proposed that the ferromagnetic bcc Fe is surrounded and interfaced with antiferromagnetic fcc Fe, as evidenced by a hysteresis shift in the FC curves.^[23] As discussed before, the formation of ferromagnetic fcc Fe is very sensitive to the synthesis conditions, and the results

presented here were obtained from CNT samples made under different conditions than those in ref. [23]. Although the hyperfine fields for fcc Fe particles measured by Mössbauer spectroscopy are coincidentally very close to those of the bcc Fe and Fe₃C phases, no diffraction peaks or patterns from bcc Fe or Fe₃C were detected in the X-ray diffraction and electron microscopy data. Hence, we conclude that the observed magnetic moments must originate from the fcc Fe₄C nanoparticles.

A lattice expansion in fcc γ -Fe can be caused by incorporation of carbon atoms in the solid. For Fe₄C solid solutions, in which carbons are in the interstitial sites inside the crystal lattice, the lattice parameter depends nearly linearly on the number of solute (C) atoms per solvent atom (Fe).^[24,25] The lattice parameter obtained from our X-ray data for the γ -Fe is 0.362–0.364 nm, which is greater than that of pure γ -Fe (\approx 0.3567 nm),^[24] thus indicating that less than 10 at% of carbon atoms are interstitially inside the Fe unit cells and therefore inducing the lattice parameter expansion.

Lattice expansion and changes in electronic structure due to interstitial carbon not only cause the stable phase formation of fcc Fe but also stabilize the ferromagnetic state, as shown by first-principles calculations based on density functional theory (Figure 3). We used both the local spin-density approximation (LSDA) and the generalized gradient approximation (GGA).^[26] The cohesive energy and the magnetic moments for pure Fe in the fcc and bcc phases are summarized in Figure 3a. The equilibrium lattice constants of pure Fe in bcc and fcc structures are 0.28 and 0.34 nm, respectively, in good agreement with the experimental values of 0.286 and 0.357 nm.^[24] The magnetic moments corresponding to the lattice parameters of 0.28 nm in bcc Fe and 0.34 nm in fcc Fe are 2.2 and \approx 0 μ B, respectively, which indicates that their ground states are ferromagnetic for bcc Fe and nonmagnetic for fcc Fe, consistent with earlier results.^[3,6,10]

The effect of carbon incorporated in the interstitial sites of the Fe lattice on the magnetic properties of the fcc phase was computationally studied using a supercell method with a carbon/iron concentration ratio of 1:4. In the fcc unit cell (schematic in Figure 3b, inset), carbon atoms are placed at octahedral interstitial sites, which have been used to study the carbon content in the fcc Fe lattice (see ref. [27] and references therein). The calculated data for the fcc Fe-C structure is shown in Figure 3b, where the lowest cohesive energy for the fcc Fe-C is -6.7 eV corresponding to a lattice constant of 0.37 nm. Compared with the results in Figure 3a, the following facts should be noted. Firstly, the cohesive energy of the fcc Fe-C structure is substantially lowered (-0.6 eV) compared to those of both the fcc and bcc structures of pure Fe; the experimental cohesive energy of graphite is very high— 716 kJ mol⁻¹ (7.4 eV atom⁻¹)—so this is not enough to provide phase stability, as is also clear from the experimental phase diagram.^[21] Secondly, the ground state for the fcc Fe-C is given for the lattice constant of 0.37 nm, which corresponds to a lattice expansion of 0.03 nm compared to 0.34 nm for pure fcc Fe. Significantly, as shown in Figure 3b, fcc Fe-C is found to be ferromagnet-

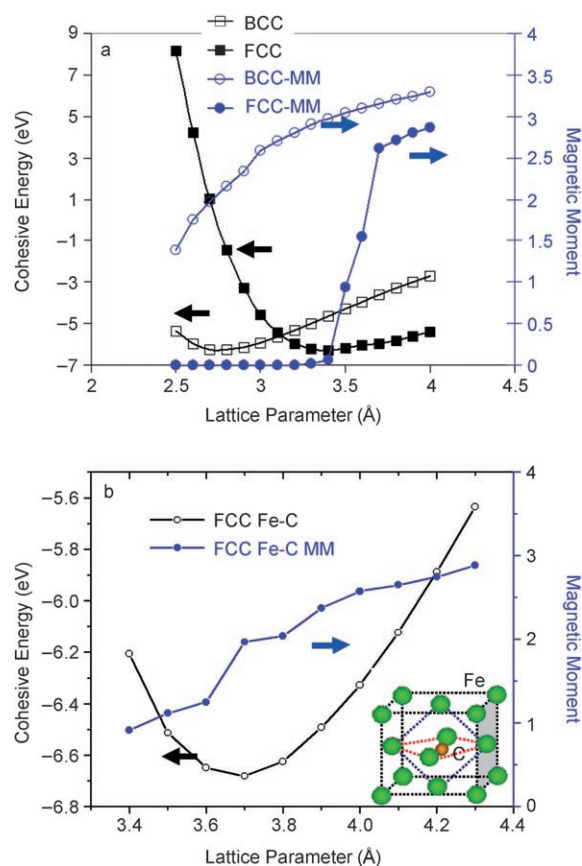


Figure 3. Theoretical calculation of the cohesive energy and magnetic moment (MM) of iron. a) Cohesive energy and magnetic moment per atom as a function of lattice parameter in the case of pure iron in fcc and bcc structures using first-principles density functional theory. The equilibrium lattice constant of iron in the bcc and fcc structures is 2.8 and 3.4 Å, respectively, while the ground states are ferromagnetic (2.2 μ B) for bcc iron and nonmagnetic (\approx 0 μ B) for fcc iron. b) Cohesive energy and magnetic moment per atom as a function of lattice parameter in fcc iron with an interstitial C atom at the body center. The equilibrium lattice constant is about 3.7 Å. The ground state of the fcc iron with carbon at the interstitial site is ferromagnetic, in perfect agreement with magnetic experimental measurements. Inset: schematic of a carbon atom at the octahedral interstitial site in the fcc unit cell used for the Fe-C calculation. Arrows guide the eye to the corresponding y axis.

ic. The nonmagnetic fcc Fe-C solution, corresponding to a lattice parameter of 0.37 nm, lies \approx 0.22 eV atom⁻¹ above the ferromagnetic phase and exceeds the Stoner criterion, thus implying magnetism $N(E_F)I=1.17 > 1$. Without carbon incorporation in the Fe lattice, the γ -Fe phase will not be stable at room temperature, even with the same lattice expansion (fcc curve in Figure 3a), which confirms the stabilization of the lattice distortion by the interstitial carbon atoms. We also performed calculations with a carbon atom at the tetrahedral interstitial site ($P(-4)3m$ space group) and found the Fe-C compound to be ferromagnetic. However, the cohesive energy in the tetrahedral case is 0.6 eV higher than that of octahedral configurations, thus ruling out the tetrahedral configuration. Widom et al.^[28] have reported a metastable Fe₄C tetrahedral configuration. We also

did calculations within a larger (eight Fe atoms) cell with a single carbon atom at an octahedral interstitial site. Again we obtained ferromagnetism, in this case with a magnetic moment of $2.27 \mu_B$.

To gain further insight into the effects of carbon atoms incorporated in γ -Fe on the onset of its magnetic moments, we calculated the partial density of states associated with the d bands of Fe atoms in the Fe-C structure (Figure 4).

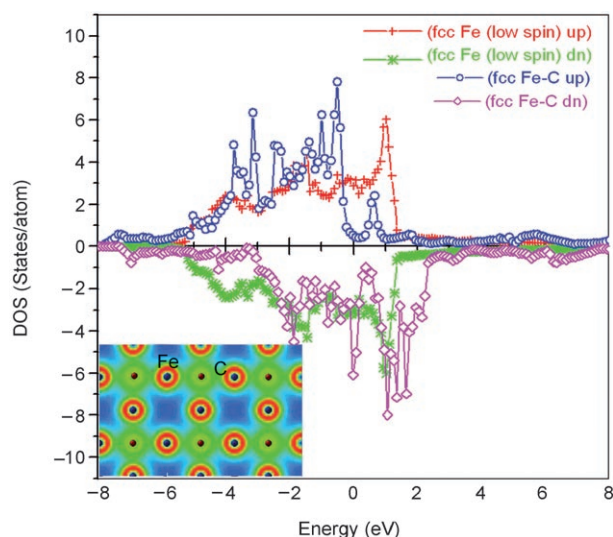


Figure 4. Theoretical calculation of spin-up (up) and spin-down (dn) partial densities of state (DOS) associated with d bands of the fcc Fe-C and pure fcc Fe structures. The d -band filling for fcc Fe-C is intermediate between those of pure fcc Fe and fcc Co due to carbon valence electrons, and is narrower than in fcc iron because of lattice expansion. Spin-down densities of state are multiplied by -1 for pictorial clarity. Inset: 2D charge-density plot obtained from the first-principles density functional calculations in the Fe-C supercell (concentration ratio between C and Fe is 1:4), which shows electron sharing between carbon and iron. The color scale goes from blue for small values, through green, to red for large values.

The d -band structure for Fe-C alloy is narrower than that for pure fcc Fe with a higher band filling. Hence, both lattice expansion due to interstitial carbon and charge sharing between carbon and iron (which is corroborated by our analysis of the charge-density plot shown in the inset of Figure 4) play a role in inducing ferromagnetism in the system. In fact, the charge sharing between the carbon and iron stabilizes the ferromagnetic phase, as seen from the cohesive energy plot shown in Figure 3. The d -band filling for fcc Fe-C is somewhat intermediate between those of pure fcc Fe and fcc Co (see Figure 4), yet it is narrower than that for pure fcc Fe because of the effect of lattice expansion. We did not perform calculations for spin-spiral states, which are known to be present in fcc Fe at lower lattice parameters,^[29] but we note that both the larger lattice parameter and the change in d -band filling (toward Co, which is ferromagnetic at room temperature) favor ferromagnetism over antiferromagnetism.

3. Conclusions

In conclusion, our experimental and theoretical studies show that the fcc Fe nanoparticles are stabilized at ambient temperatures because of carbon atoms incorporated in the interstitial sites of the fcc Fe lattice. The interstitial atoms produce lattice expansion and changes in electronic structure that stabilize a high-spin ferromagnetic phase. The room-temperature magnetic measurements on these samples provide direct evidence that the fcc Fe nanoparticles are ferromagnetic, and the magnetic moment observed in this structure is supported by our first-principles theoretical prediction.

4. Experimental Section

The three-dimensional arrays of carbon nanotubes, in which iron particles were trapped, were grown in a CVD tube-furnace system from a vapor-phase mixture of xylene (C_8H_{10}) and ferrocene ($Fe(C_5H_5)_2$). The CVD chamber was pumped down to 10^{-3} Torr, backfilled with a flow of argon gas at ≈ 100 mTorr, and gradually heated up to $800^\circ C$. A solution of ferrocene (0.01 g mL^{-1} ; nanotube nucleation initiator with Fe) in xylene (carbon source), which was preheated at $\approx 150^\circ C$ and sublimed into the CVD chamber, produced vertically aligned multiwalled nanotubes (MWNTs) tens of micrometers in thickness and 20–30 nm in diameter, grown on polished SiO_2 surfaces. The average center-to-center spacing between adjacent nanotubes in these samples was ≈ 50 nm. The reaction was terminated by introducing argon gas and cooling the furnace to room temperature under an argon atmosphere. For more information, please refer to refs. [17, 30].

To confirm that the measured magnetization comes solely from the trapped fcc iron nanoparticles, magnetic measurements were performed on two other types of samples: one was a random-oriented MWNT powder produced with the arc-discharge technique (no catalyst in pristine sample); the other consisted of aligned MWNT arrays synthesized by the CVD method, with the iron catalyst removed by annealing the pristine sample at $1900^\circ C$ in a vacuum. No iron particles were found in the annealed sample, as deduced from TEM observations. No magnetization was observed for these samples, which indicates that the ferromagnetic behavior is solely from the magnetic moments of the Fe nanoparticles.

To determine the ground-state structure and magnetic properties, Vanderbilt-type ultrasoft pseudopotentials were used to describe electron–ion interactions. For the bulk calculation (both fcc and bcc phase) of iron, we used a plane-wave cutoff of 21 Ry. The Brillouin zone was sampled with a $15 \times 15 \times 15$ Monkhorst–Pack grid. The VASP code^[31] was used for the calculation. Full-potential linearized augmented plane-wave (FLAPW) calculations were used for some of our calculations to confirm the accuracy of our results obtained by the pseudopotential approach. The convergence threshold in electronic energy during the self-consistent procedure was set to be 1×10^{-5} eV. The GGA calculation (not shown here) can provide more quantitative information

on the stability of these phases, which arises due to a small difference in the cohesive energies between iron atoms in the fcc and bcc phases. However, here we emphasize the LSDA results because the GGA is known to sometimes overestimate magnetization. To evaluate the effect of carbon incorporated in the interstitial sites of the Fe lattice on the magnetic properties of the fcc phase, a supercell method with a carbon/iron concentration ratio of 1:4 was employed. Basically, we created the band structure by repeating the unit cell. As we placed carbon here, we carried out the calculation by repeating the cell that contained both iron and carbon.

Acknowledgements

The authors thank Prof. M. Shiga and Prof. G. V. S. Sastry for valuable comments, and Prof. C. A. Ross for the use of the AGM for magnetization measurements. B.W., P.M.A., R.P., and S.K.N. acknowledge financial support from the RPI NSF NSEC on directed assembly of nanostructures, Philip Morris USA, and the ACS Petroleum Research Fund (R.P. and S.K.N.). B.W. is also grateful for an AML/NIMS COE research project at NIMS, Japan.

-
- [1] L. Kaufman, *Acta Metall.* **1959**, *7*, 575–587.
 [2] V. L. Moruzzi, P. M. Marcus, K. Schwarz, P. Mohn, *Phys. Rev. B* **1986**, *34*, 1784–1791.
 [3] G. L. Krasko, *Phys. Rev. B* **1987**, *36*, 8565–8569.
 [4] M. Shiga, *J. Phys. Soc. Jpn.* **1967**, *22*, 539–546.
 [5] See, for instance: R. M. Bozorth, *Ferromagnetism*, IEEE Press, Piscataway, NJ, **1951**.
 [6] C. S. Wang, B. M. Klein, H. Krakauer, *Phys. Rev. Lett.* **1985**, *54*, 1852–1855.
 [7] L. Kaufman, E. V. Clougherty, R. J. Weiss, *Acta Metall.* **1963**, *11*, 323–335.
 [8] F. J. Pinski, J. Staunton, B. L. Gyorffy, D. D. Johnson, G. M. Stocks, *Phys. Rev. Lett.* **1986**, *56*, 2096–2099.
 [9] A. Kirilyuk, J. Giergiel, J. Shen, M. Straub, J. Kirschner, *Phys. Rev. B* **1996**, *54*, 1050–1063.
 [10] J. Thomassen, F. May, B. Feldmann, M. Wuttig, H. Ibach, *Phys. Rev. Lett.* **1992**, *69*, 3831–3834.
 [11] M. Stampanoni, A. Vaterlaus, M. Aeschlimann, F. Mejer, *J. Appl. Phys.* **1988**, *64*, 5321–5324.
 [12] C. E. Guillaume, *C. R. Acad. Sci.* **1897**, *125*, 235–238.
 [13] M. van Schilfhaarde, I. A. Abrikosov, B. Johansson, *Nature* **1999**, *400*, 46–49.
 [14] X. X. Zhang, G. H. Wen, S. M. Huang, L. M. Dai, R. P. Gao, Z. L. Wang, *J. Magn. Magn. Mater.* **2001**, *231*, L9–L12.
 [15] J. Jiao, S. Seraphin, X. Wang, J. C. Whithers, *J. Appl. Phys.* **1996**, *80*, 103–108.
 [16] N. Grobert, W. K. Hsu, Y. Q. Zhu, J. P. Hare, H. W. Kroto, D. R. M. Walton, M. Terrones, H. Terrones, P. Redlich, M. Ruhle, R. Escudero, F. Morales, *Appl. Phys. Lett.* **1999**, *75*, 3363–3365.
 [17] B. Q. Wei, R. Vajtai, Y. Jung, J. Ward, R. Zhang, G. Ramanath, P. M. Ajayan, *Chem. Mater.* **2003**, *15*, 1598–1606.
 [18] Y. Tsunoda, *J. Phys. Condens. Matter* **1989**, *1*, 10427–10438.
 [19] X. Zhang, A. Y. Cao, B. Q. Wei, Y. H. Li, J. Q. Wei, C. L. Xu, D. H. Wu, *Chem. Phys. Lett.* **2002**, *362*, 285–290.
 [20] H. Kim, M. J. Kaufman, W. M. Sigmund, D. Jacques, R. Andrews, *J. Mater. Res.* **2003**, *18*, 1104–1108.
 [21] *Binary Alloy Phase Diagrams* (Ed.: T. B. Massalski), ASM International, Materials Park, OH, **1990**.
 [22] T. Hinomura, S. Nasu, *Nuovo Cimento D* **1996**, *18*, 253–257.
 [23] C. Prados, P. Crespo, J. M. González, A. Hernando, J. F. Marco, R. Gancedo, N. Grobert, M. Terrones, R. M. Walton, H. W. Kroto, *Phys. Rev. B* **2002**, *65*, 113405.
 [24] M. Onink, C. M. Brakman, F. D. Tichelaar, E. J. Mittemeijer, S. van der Zwaag, *Scripta Metall. Mater.* **1993**, *29*, 1011–1016.
 [25] C. M. Li, F. Sommer, E. J. Mittemeijer, *Z. Metallkd.* **2000**, *91*, 5–9.
 [26] J. P. Perdew, J. A. Chevary, S. H. Vosko, K. A. Jackson, M. R. Pederson, D. J. Singh, C. Fiolhais, *Phys. Rev. B* **1992**, *46*, 6671–6687.
 [27] K. F. Laneri, J. Desimoni, G. J. Zarragoicoechea, A. Fernandez-Guillermet, *Phys. Rev. B* **2002**, *66*, 134201.
 [28] M. Widom, L. Xie, S. Naidu, M. Mihalkovic, D. M. Nicholson, Y. Wang, “First Principles Simulation of Iron-Based Intermetallic Alloys”, www.euler.phys.cmu.edu/widom/pubs/pubs.html (accessed on: March 17, 2006).
 [29] E. Sjostedt, L. Nordstrom, *Phys. Rev. B* **2002**, *66*, 014447, and references therein.
 [30] B. Q. Wei, R. Vajtai, Y. Jung, J. Ward, Y. Zhang, G. Ramanath, P. M. Ajayan, *Nature* **2002**, *416*, 495–496.
 [31] G. Kresse, J. Furthmüller, *Phys. Rev. B* **1996**, *54*, 11169–11186.

Received: November 9, 2005
 Published online on April 7, 2006